# Exoplanet imaging performance envelopes for starshade-based missions

**Eliad Peretz[o],[a],\* Kevin Hall,[b] John C. Mather[o],[a] Stuart Shaklan[o],[c] and Sergi Hildebrandt[o][c]**

aNASA Goddard Space Flight Center, Greenbelt, Maryland, United States
bUniversity of Maryland, College Park, Department of Astronomy, College Park, Maryland, United States
cJet Propulsion Laboratory, California Institute of Technology, Pasadena, California, United States

**Abstract.** We lay out the capabilities and limitations of starshade-based missions aiming to measure the reflected light spectra of temperate planets from an imaging perspective. We use the Starshade Imaging Simulation Toolkit for Exoplanet Reconnaissance to conduct high fidelity end-to-end optical simulations, taking a step forward from simplified analytical equations, exploring and quantifying the impact of an array of observational conditions, including natural parameters such as target star types, planet types, distances, planet phases, and exo-zodiacal dust, and starshade perturbations such as tilt, shift off line of sight, edge errors, and glint. We find that signal-to-noise ratio (SNR) requirements used for establishing detection and spectral characterization, is not suitable under realistic observation conditions for a wide range of targets. We show that even if we assume that the spatially distributed, time-varying background noise could be known and calibrated to a level of 1%, each target star will need its own SNR requirement based on its unique observation conditions, nearly always resulting in a higher threshold SNR, with values as high as X5 from currently established requirement, and in some cases impossible to detect. We conduct statistical analysis using end-to-end optical simulations, taking into account observationally based priors and update previously established completeness values for an array of target stars and mission configurations, accounting for starshade perturbations, and background knowledge at a level of one percent and find that completeness values are negatively impacted and reduced by up to 50% across targets even at ranges shorter than 10 pc. Finally, we utilize information from over hundreds of thousands of detailed imaging simulations to map accessible target stars for both optimistic and pessimistic scenarios, reassessing the expected capabilities of starshade-based high contrast direct imaging missions. © *The Authors. Published by SPIE under a Creative Commons Attribution 4.0 Unported License. Distribution or reproduction of this work in whole or in part requires full attribution of the original publication, including its DOI.* [DOI: 10 .1117/1.JATIS.7.2.021215]

## 1 Introduction

As exoplanets are detected and confirmed in increasing numbers, the exoplanet science community is able to broaden their scope from individual planet characterization to exoplanet demography. However, typical indirect detection methods provide an incomplete census, leading to uncertainty of the conditions under which such systems will be required to be imaged and spectrally characterized. Direct imaging could expand the detection coverage to create a more complete survey due to its unique sensitivity to planets at relevant angular separations, masses, and radii, among other properties. These insights are crucial for science questions of formation, dynamical evolution, and population-scale demographics, all of which are key for elucidating our Solar System's place within the larger exoplanet population, and are steps toward addressing questions of the uniqueness and potential habitability of Earth-like planets.[1]

---

\*Address all correspondence to Eliad Peretz, eliad.peretz@nasa.gov

Starshades[2,3] and coronagraphs[4,5] have been identified as suitable technologies that can achieve the necessary degree of starlight suppression[6] at the relevant separations[7] that could enable the direct imaging of temperate planets around sun-like stars.

This work explores the capabilities and limitations of starshade-based exoplanet observations from an imaging perspective, taking both space and ground-based opportunities into consideration.

We examine three proposed starshade-based solutions: (1) starshade rendezvous, a starshade-based mission proposed to work with the Nancy Grace Roman Space Telescope (NGRST),[8] (2) the Habitable Exoplanet Observatory (HabEx) starshade,[9] and (3) the Remote Occulter (R-O)[10–13] proposed to work with future Extremely Large Telescopes (ELT).

We study how changes of both observational parameters (properties of the imaged planet, its star, and its astrophysical context) and system parameters (properties of the starshade and telescope) affect end-result imaging capabilities for each mission by utilizing the Starshade Imaging Simulation Toolkit for Exoplanet Reconnaissance (SISTER).[14]

In Sec. 2, we present, in short, the methods used to conduct imaging simulations in this paper. In Sec. 3, we explore how individual natural parameters will impact the imaging capabilities. In Sec. 3.1, we examine the impact of the chosen star types and distances for an array of planets; in Sec. 3.2, we consider the effects of observing planets at unknown phases; in Sec. 3.3, we continue to investigate the effects of exo-zodiacal dust, its peak radius and other phenomena; finally, in Sec. 3.4, we study a variety of planets' semi-major axes, albedos, and radii.

In Sec. 4, we consider how major individual starshade perturbations and shape changes driven by thermal, mechanical, and other nonideal phenomena could impact the imaging quality. We explore the impact of a starshade tilt relative to the line of sight (Sec. 4.1); we follow on to study off-line-of-sight shifts due to misalignment in formation flight (Sec. 4.2), glint caused by the sun illuminating the petal edges (Sec. 4.3), and petal edge errors (Sec. 4.4).

Finally, while in the previous sections, we presented the impact of individual parameters, in Sec. 5, we integrate them, review our findings, and provide interpretation and analysis. We begin by providing a performance envelope used to probe which target stars could be observed under optimistic and pessimistic observational scenarios (Sec. 5.1); we then continue to examine the impact of an observer capability to accurately subtract the background noise to a given level of accuracy (Sec. 5.2), followed by a reassessment of the completeness values for target stars using realistic observation conditions (Sec. 5.3); and conclude with future work (Sec. 5.4).

## 2 Imaging with SISTER

In this section, we provide a short introduction to how SISTER-simulated images are generated and analyzed in this paper. SISTER allows us to take a step further from existing analytical exposure time calculators and better estimate the optical performance of starshade-based missions. It produces high fidelity simulations of directly imaged exoplanetary systems by considering the specific starshade design, end-to-end optical/telescope configurations including its optical subsystems, and the diverse landscape of exoplanetary systems and their parent stars. It does so by deriving the optical response of the starshade-telescope system. SISTER derives the optical response using boundary diffraction modeling, calculating the Point Spread Function (PSF) spatial response.[15] These methods have been verified against experimental results to a level of $10^{-10}$ contrast, and then compared to other independent modeling tools and has been found to agree within 1%. For further details regarding the inner working of the simulations including all features and parameters provided by SISTER refer to the handbook.[16]

To illustrate the modeling and analysis process conducted by us for each simulation, we present imaging simulations for Tau Ceti, a G8V star only 3.6 pc away, and a prime target for many direct imaging missions. We assume a hypothetical Earth-like planet is positioned at 0.7 AU, with a 45-deg phase, and an exozodi factor of 4.5, where the solar system zodiacal dust is also included. For each simulation, we show the true detector pixel image (non-post processed/adapted/color image) at the 600 to 800 (nm) band, and present the planet signal and background noise. We then extract for each simulation the noise and the signal from the planets, and compute their signal-to-noise ratio (SNR) as can be seen in Fig. 1.
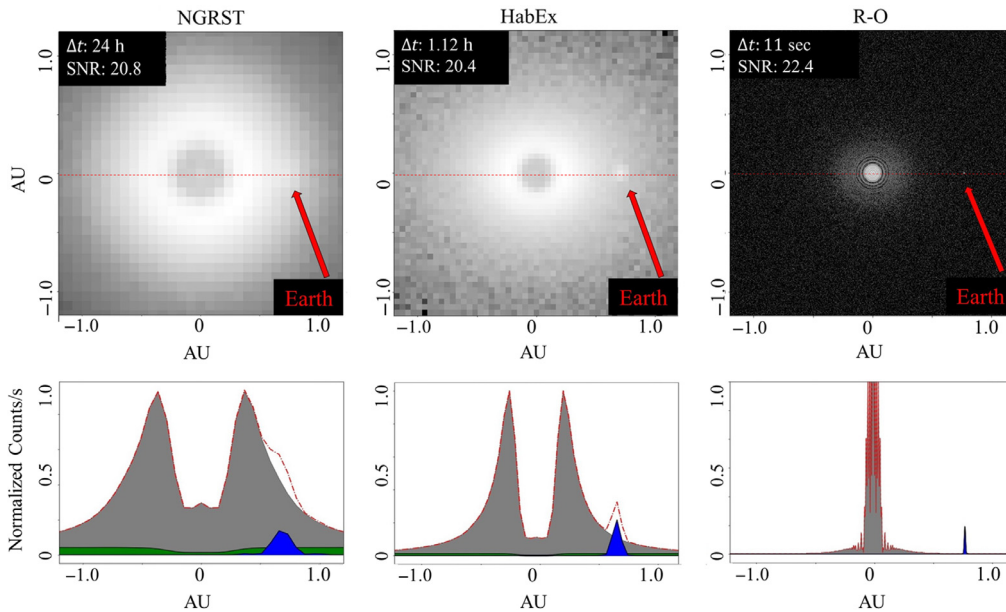
**Fig. 1** In this figure, we display simulations of the Tau Ceti system using SISTER for all three starshade missions. Each simulation output is broken down into two images: The raw science image, and the curves from each flux component that join together to build the final simulation output. The raw science images can be seen on the top row, and an arrow points to the location of the Earth-like planet. The exposure time and resulting planet SNR can be seen in the top left of each image. In the bottom row, the individual flux components can be identified by three different colored regions. The gray region contains the combined background flux from excess light from the target star, exozodiacal dust within the system, and random noise generated within the detector. The green region contains the flux from the local zodiacal dust within the Solar System, and the blue region contains the total flux from the Earth-like planet. The two dashed red lines in the top and bottom images are equivalent; it indicates the readout flux (detector pixel read). Solar glint was not included for these simulations to allow for favorable conditions.

We also provide for each one of the images the exposure time, SNR, and a visual indicator of the planet location. Under each image, a cross-section is presented, indicating the background in gray, the signal in blue, and the total signal in a red dashed line, all normalized to the photon count of the signal peak.

## 3 Natural Parameters Effects on Imaging capabilities

In this section, we explore a range of individually varying natural parameters to better understand how they shape the imaging and detection capabilities of starshade-based missions and potentially their design and operations. While this paper concludes in Sec. 5 with a discussion and recommendations for SNR requirements, we open our analysis by adopting missions' minimum detection threshold requirement of SNR = 7 to facilitate the discussion.[9] Our individual system parameters are chosen by relying upon observationally based priors,[17] and Table 1 summarizes all parameters. For further details regarding the system parameters utilized in our analysis, see Appendix B.

### 3.1 *Star, Planet Types and Ranges*

In this section, we explore which star and planet types and distances, are accessible for starshade-based missions. To establish representative exposure times for the case of an Earth-like planet and other Solar System planets, placed in their respective orbits of scaled to the star luminosity. We are interested in determining the relationship between exposure time and target distance such that an SNR of 7 can be obtained, for star distances of 3 to 25 pc and exposure times of up to 24 h, for different planet types and we present the results at Fig. 2.

**Table 1** List of all priors used for our simulations. All distributions within the square brackets are uniform. The outputs are not necessarily uniform. For Inclination, the distribution alters once the cosine function is applied.

| Parameter | Distribution |
| --- | --- |
| Eccentricity | [0, 0.3] |
| Planet Radius | $[0.6, 1.4] R_\oplus$ |
| Semi-major Axis | $[0.7 - 1.67 \text{ AU}] \sqrt{L_*}$ |
| Inclination | $\cos[-1,1]$ |
| Albedo | [0.1, 0.5] |
| Exozodi | [1, 21] |
| Argument of Periapsis | [0 deg, 360 deg] |

We extract from Fig. 2 representative exposure times for the three missions, such that 85% of target distance are covered for each star type: (1) 24 h for NGRST, (2) 10 h for HabEx, and (3) 30 min for R-O. The imaging bands for each mission are 615 to 800 nm for NGRST, and 600 to 800 nm for HabEx and R-O. From this section forward, these exposure times and bands will be used throughout the paper unless specifically stated otherwise.

In Fig. 3, we display the imaging simulations for F5V-G5V-K5V-M0V stars, for a Venus-Earth-Mars-Jupiter-Saturn system at a distance of 8 pc, with an exo-zodi level of 4.5, and an inclination of 0 deg. For each of the twelve images, we provide the exposure time and resultant SNR for every one of the planets. These analyses are conducted assuming an infinite outer working angle (OWA).

We finalize this section by combining in Fig. 4, a map that accommodates all main sequence GAIA stars within 25 Pc, as a function of the target star distance and luminosity. We then project the starshade angular size for each mission, such that all observable target stars could accommodate viewing an Earth-like planet at 1 AU, scaled to the star luminosity. We then mark the distance at which each mission could reach an SNR of 7 as a function of a target star luminosity and distance. This identifies which stars could be observed by each mission given the allotted exposure time.

Figure 4 will evolve as we account for additional parameters such as planet phases in Fig. 6, exo-zodiacal dust in Fig. 10, and starshade perturbations in Fig. 17 to show the change in accessible target stars as each parameter is accumulated.

## 3.2 Planet Phase

In this section, we present the imaging detection sensitivity to the planet phase when observed, driven by the Keplerian motion of the planet and the system inclination relative to the line of sight. In Fig. 5, we show for four target stars at different distances, the regions in which SNR is smaller than 7 as a function of system inclination and the planet argument of periapsis (phase).

Phase completeness, which in this paper indicates the chance an observer could reach an SNR of 7 at the allotted exposure time for a random planet phase, is a useful quantity that is taken into account where the observer is interested in maximizing the chance to observe a target. Therefore, we repeat the analysis conducted in Fig. 4 for the relevant statistical distribution of system inclinations, but now project for each mission the curves for a phase completeness value of 0.35 as can be seen in Fig. 6.

The curves for each mission indicate which luminosity and distances are within reach if such a requirement is imposed; the completeness curves that are presented in this figure will evolve throughout the paper as more natural, and system parameters will be taken into account to reflect the impact each parameter will have on this map.
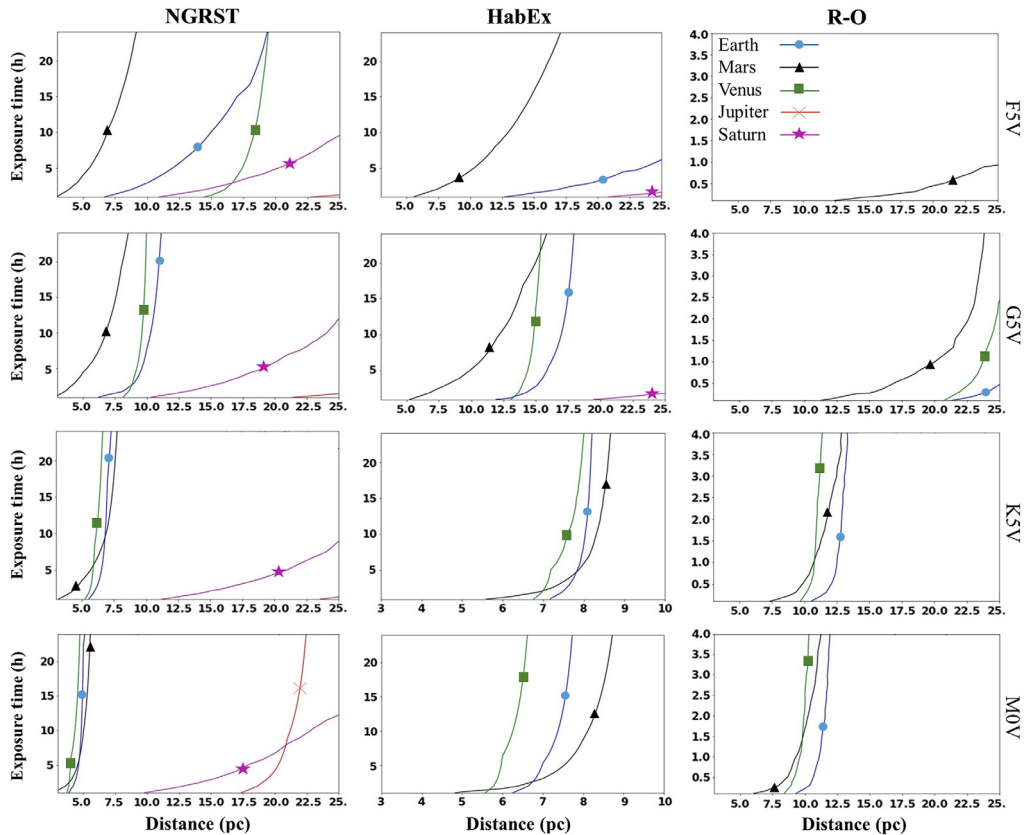
**Fig. 2** Exposure time required to reach an SNR of 7 as a function of distance for each mission and star type: The black, blue, green, red, and purple curves correspond to Mars, Earth, Venus, Jupiter, and Saturn, respectively. Each planet has their orbit scaled by the luminosity of each star type. The exozodi factor was set to 0 for these simulations, and the local zodiacal dust present within the solar system was applied to add an additional realistic background flux source. Solar glint was not used for these simulations. If a curve for one of the planets is not shown, then it is able to maintain an SNR > 7 for the all distances and exposure times displayed in the figure.

## 3.3 *Exo-zodi Dust and Resonant Dust Rings*

Exo-zodiacal dust could become a major noise source and interfere with the imaging of exoplanets.[18] This could be further complicated by dust structures in the observed system[19,20] as is evident by both the leading and trailing dust clumps near Earth. We first investigate the case of a symmetric disk, with a half peak brightness at 0.1 AU, similar to our own solar system. We open by maintaining such favorable assumptions and examine how the regions in Fig. 7 will change for the nearby target star Zeta Tucanae, which has a corresponding Hipparcos catalog ID of HIP 1599 for exo-zodi levels of 0, 3, 11.8, and 21, which represent a no noise, optimistic median, pessimistic median, and the $3\sigma$ optimistic scenario value respectively from the latest HOSTS survey[21] and present the results in Fig. 7.

We then further explore symmetrically distributed dust cloud with exo-zodi half peak brightness distances spanning from 0.1 to 1.5 AU, and exo-zodi levels of 0 to 50 while indicating where an SNR of 7 could be obtained, for HIP 1599 seen in Fig. 8.

We continue to introduce a clump-like structure, located in close proximity to the trailing edge of earth and show for the three missions imaging simulations for a planet only, clump only, and the two combined in Fig. 9.

Finally, in Fig. 10, we compile optimistic and pessimistic dust level scenarios and present their impact on Fig. 6. The optimistic and pessimistic dust levels are set to 3 and 11.8, respectively.
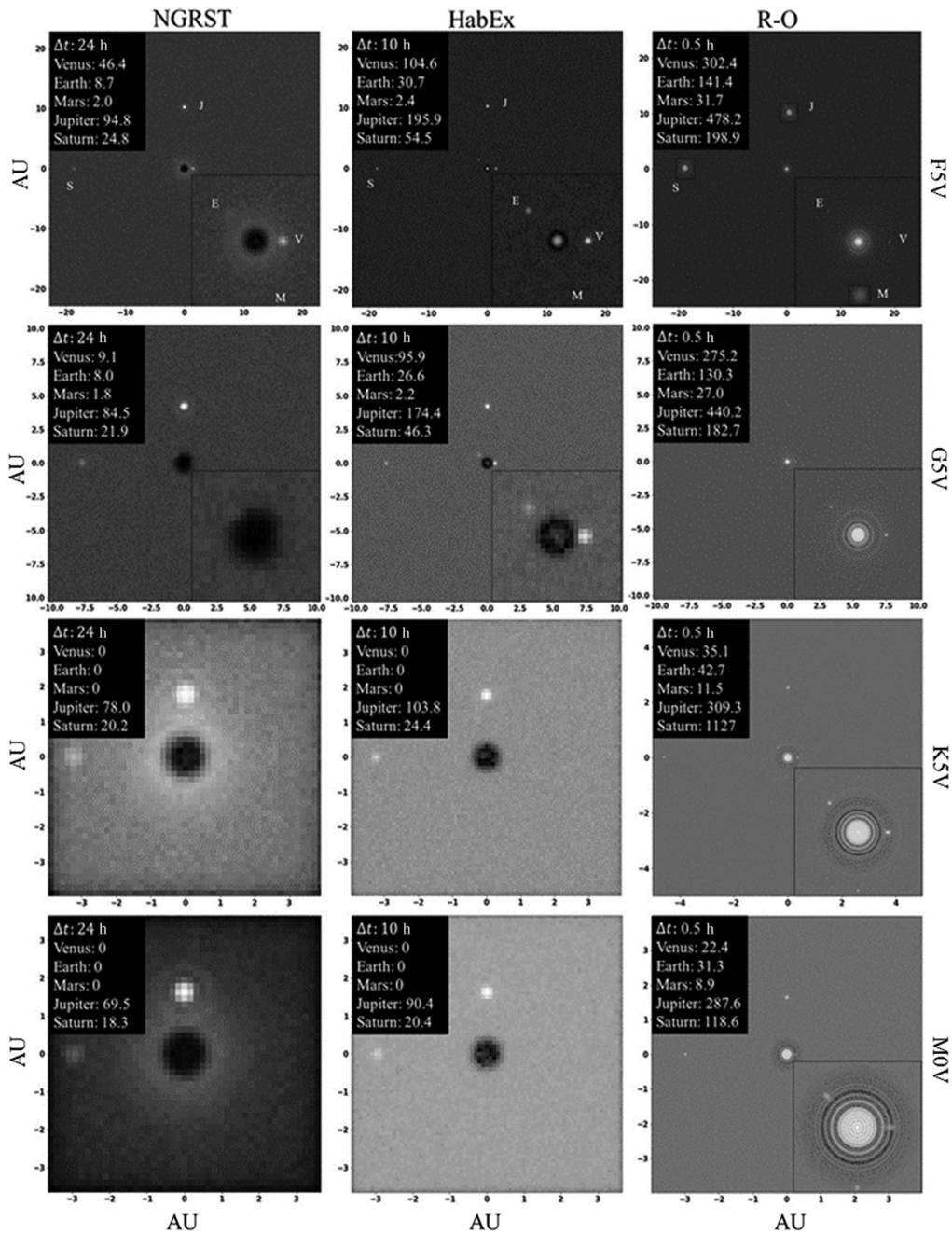
**Fig. 3** This figure explores how the Solar System would appear through each starshade mission and with four different host stars that have an exozodiacal dust disk 4.5 times the brightness of the local zodiacal dust around the Sun. Each system possesses Venus, Mars, Earth, Jupiter, and Saturn; their relative positions are labeled in the top row and are held constant for all proceeding rows. The broadband SNR is provided for all planets at the top left of each image and the exposure time. If the inner solar system planets have an SNR > 7, we provide a closer look in the bottom-right corner of the image to clearly identify the planets. The top-right image provides a closer look for both Jupiter and Saturn because the strong angular resolution makes it difficult to identify the outer planets. Each column corresponds to one of the starshade missions: NGRST, HabEx, and R-O, respectively, and each row corresponds to a different star spectral type: F5V, G5V, K5V, and M0V, respectively. As the host star brightness decreases, the planets' semi-major axis grows smaller due to the luminosity scaling $\sqrt{L_{star}}$. The horizontal and vertical axes are in units of Astronomical Units (AU). Solar glint was not included within these simulations.
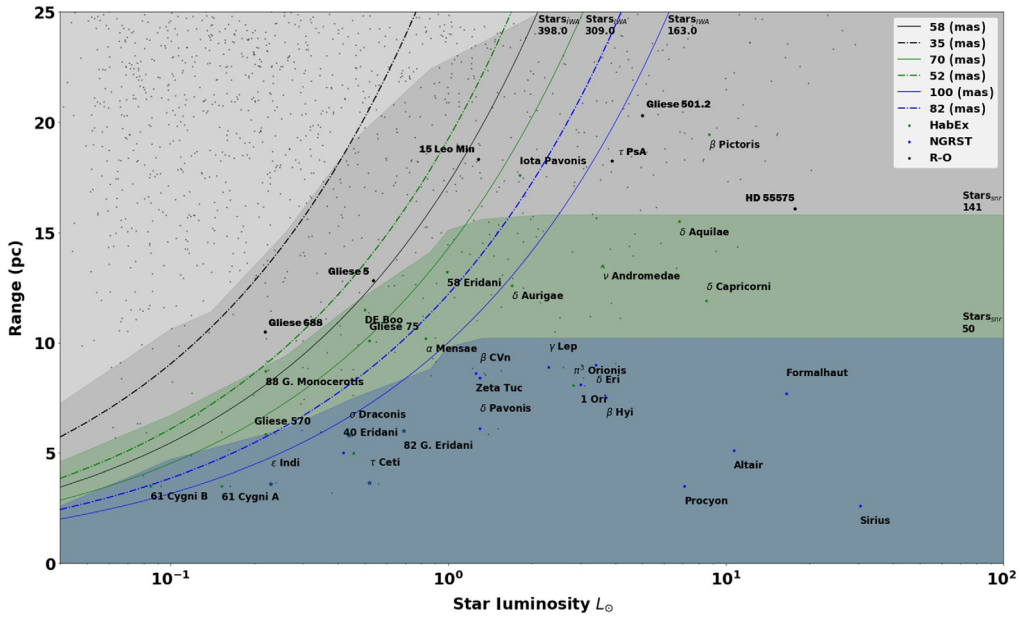
**Fig. 4** Accessible target stars for each mission, for the allotted exposure time, SNR = 7, and starshade Inner Working Angle (IWA): The black, green and blue curves correspond to R-O, HabEx, and NGRST, respectively. Solid curves correspond to each mission starshade IWA for a planet positioned at 1 AU scaled to the star luminosity. The colored regions correspond to the distance at which an Earth-like planet has an SNR equal to 7 for each mission. We provide for context stars from the Gaia DR2 in gray to identify where stars are located, and the names of stars selected as potential targets for starshade missions, and the total number of stars that have habitable zones outside of the IWA of each starshade mission at the top of the image, and the number of stars within the SNR = 7 curve on the right side of the image.
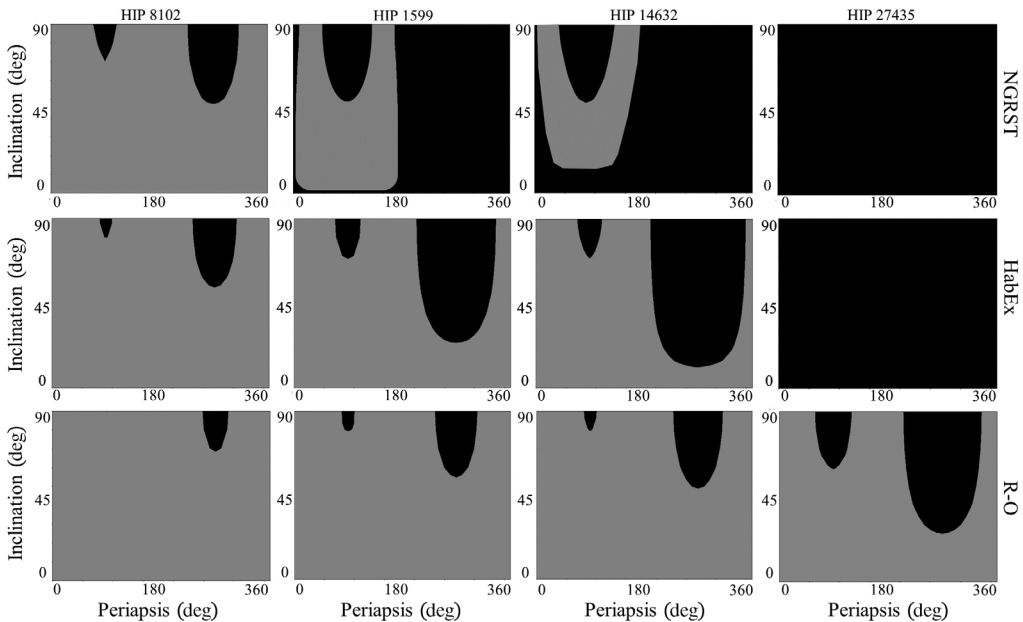


**Fig. 5** Earth-like planet observability as a function of phase for the three missions for four target stars: Each map is constructed of ~500 independent imaging simulations. In each map, the vertical axis corresponds to the orbital inclination in degrees. 0 deg represents a system that is face-on with respect to the observer, and 90 deg is edge-on. The horizontal axis is the planet's argument of periapsis in degrees. There are two regions present in every image; regions in gray identify where the planet reaches an SNR ≥ 7, and black regions identify where it cannot maintain an SNR of 7.
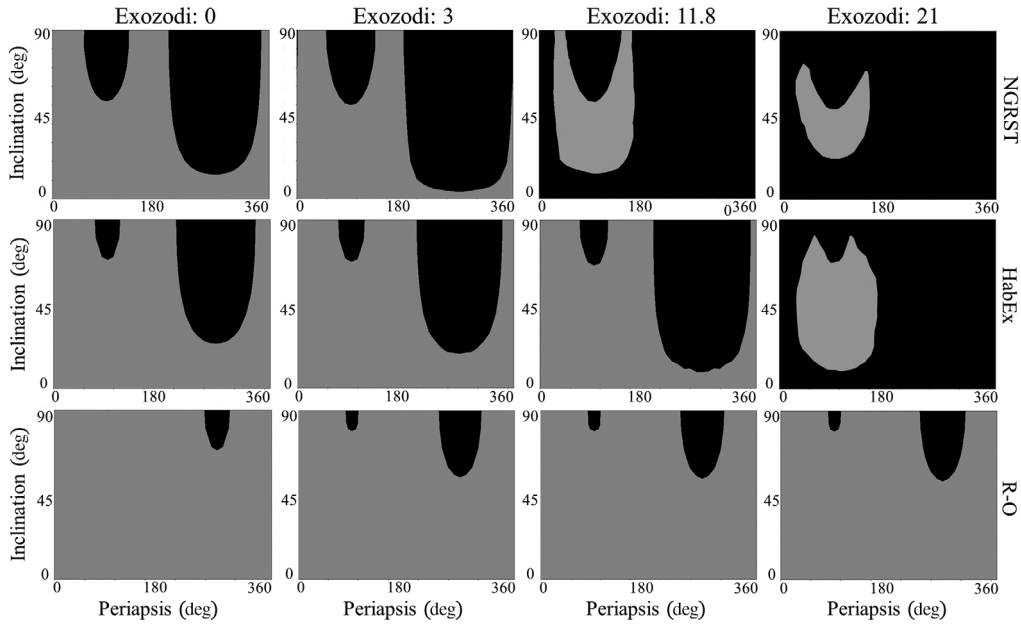
**Fig. 6** Accessible target stars for each mission, for the allotted exposure time, where the phase completeness is larger than 0.35: The black, green and blue curves correspond to R-O, HabEx, NGRST, respectively. Solid curves correspond to each mission starshade IWA for a planet positioned at 1 AU scaled to the star luminosity. The dashed lines correspond to the distance at which an Earth-like planet has a completeness of 0.35 for each mission. We provide for context stars from the Gaia DR2 in gray to identify where stars are located, the names of stars selected as potential targets for starshade missions, the total number of stars that have habitable zones outside of the IWA of each starshade mission at the top of the image, and the number of stars within phase completeness requirement curve on the right side of the image. The semi-major axis remains constant at 1 AU scaled by luminosity, the planet radius is set to $1R_{\oplus}$, planetary albedo is set to 0.3, and the exozodi factor is set to 0.

## 3.4 *Planet Radius, Albedo, and Semi-Major Axis*

In this section, we consider how predictions for the expected planet radius, semi-major axis, and albedo of the observed planets could impact the detection of such planets. Figure 11 shows for the three missions for cross-correlations the regions in which SNR = 7 can be obtained. In the first row, we explore the planet radii and semi-major axis dependence. In the second row, we pair the semi-major axis with the planetary albedo, and the third row explores the dependence on planetary albedo and radius. Finally, the fourth row intertwines both the planetary radius and semi-major axis and identifies the required albedo to maintain an SNR = 7 for each pair.

## 4 Starshade Perturbations and Their Effects on Imaging Capabilities

In previous sections, our imaging simulations assumed a near perfect starshade-telescope system, yet in reality errors introduced to the shape of the starshade caused by thermal, mechanical and an array of other phenomena may degrade the performance of the starshade. In this section we analyze some of the major perturbations that could degrade starshade-based mission performance.

## 4.1 *Tilt*

For each mission, we conduct an array of imaging in this section we conduct simulations spanning from 0 deg to 50 deg tilts, as can be seen in Fig. 12, and provide the resultant SNR for an Earth-like planet located 1 AU from the star, aligning the maximal light leakage such that it is placed as close as possible to the planet position, as a worst case scenario.

**Fig. 7.** For all three starshade missions, four different exozodi factors have been applied to the HIP 1599 system, a G0V star 8.6 pc away: 0, 3, 11.8, and 21. We identify how these exozodi levels effect the regions identified in Fig. 5. Each column corresponds to one of the four exozodi levels, and each row corresponds to one of the three starshade missions. Similar to Fig. 5, the horizontal axis is the argument of periapsis in degrees for the planet, and the vertical axis is the orientation of the system. The exozodiacal dust disk maintains the same inclination as the orbital plane. The local zodiacal dust remains constant for all simulations. The solar glint is not activated for these simulations. About ~600 individual imaging simulations were performed to build each map.
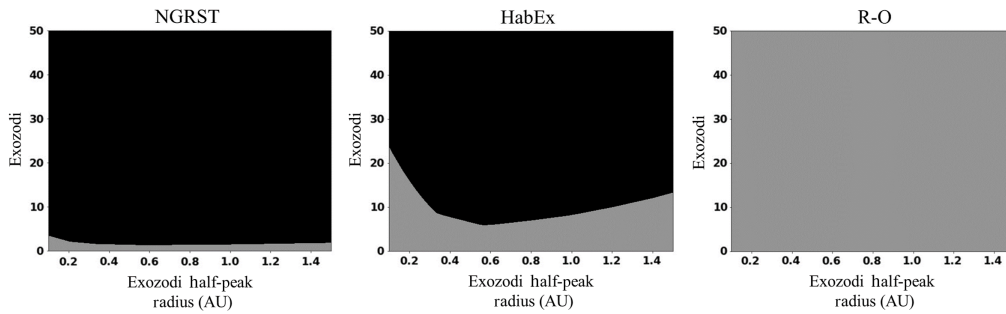


**Fig. 8** This figure explores how the exozodi factor and exozodi dust distribution effects the SNR performance for an Earth-like planet orbiting the habitable zone of Zeta Tucanae, which is 8.6 pc away and is a G0V star. For other simulations that include exozodiacal dust, the distance from the star where half of the peak intensity occurs is 0.1 AU, and it is scaled by the luminosity of the star. This figure spans this distance from 0.1 to 1.5 AU, and it spans across the horizontal axis. The vertical axis is the exozodi factor. Similar to the figures above, we divide each map into the two regions. The gray regions correspond to areas that yield an SNR larger than 7 and the black regions yield SNR values below 7. The phase of the planet remains constant at 90 deg. local zodiacal dust is present in all simulations and remains constant. Solar glint was not activated for these simulation runs. The order of the three images from left to right are NGRST, HabEx, and R-O.

## 4.2 Off- Line of Sight Error

One of the challenging aspects of starshade-based missions is the tight formation flight requirement which have been identified as a key target for the S5 program. In Fig. 13, we evaluate for the three missions the impact of non-ideal flight formation where the starshade deviates from the line of sight (LOS).
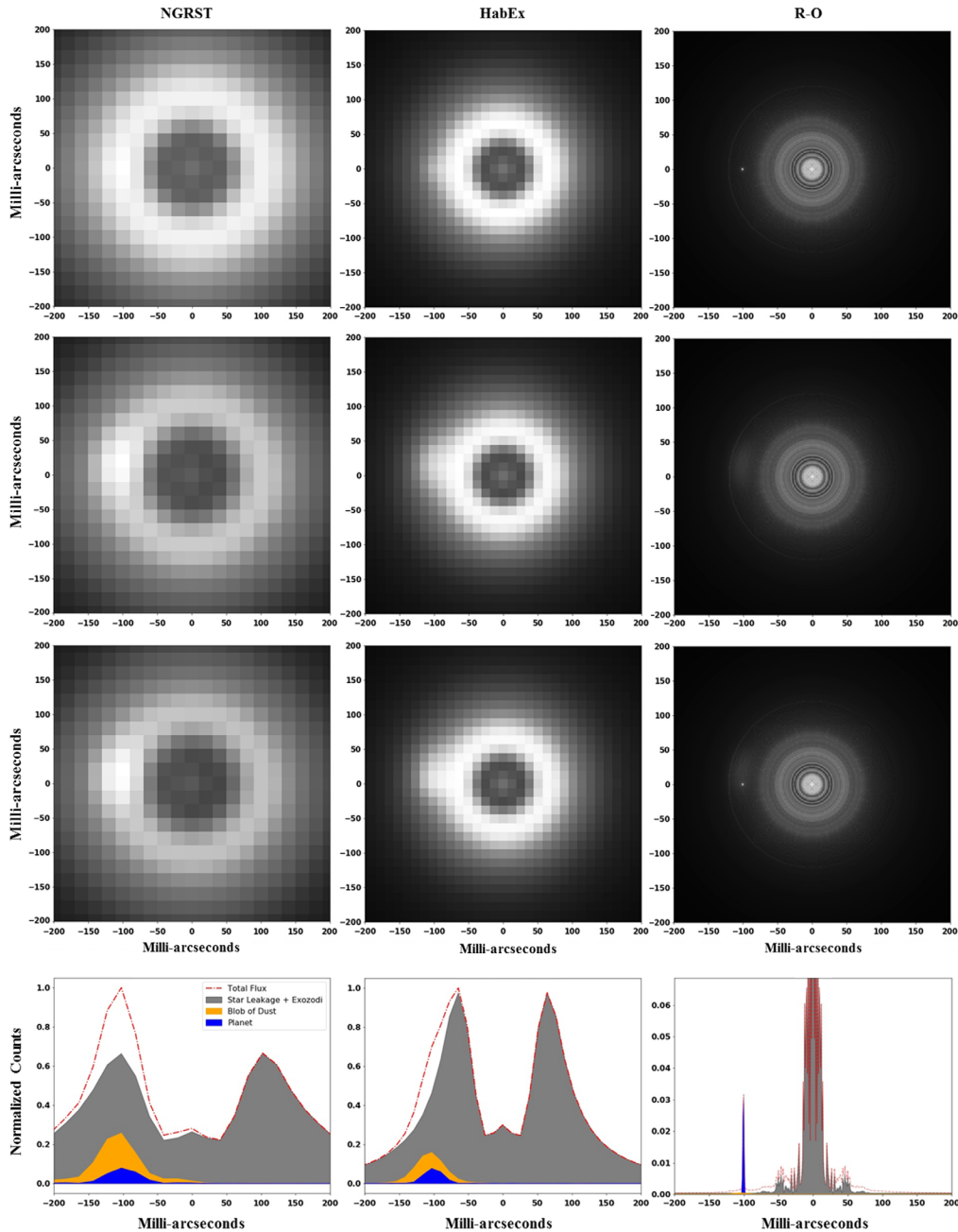
**Fig. 9** This figure examines on how a trailing blob of dust can impact the detection of Earth-like exoplanets for all starshade missions. The top row displays simulations of the Sun 10 pc away with exozodiacal dust and Earth in orbit at 1 AU. The second row replaced Earth with a trailing blob of dust, and the third row adds both the Earth and the blob of dust. The fourth row plots each flux component, as seen previously in Fig. 1, when both the planet and the blob of dust are present, but it is centered on the location of the planet. The brightness of the trailing dust blob was set to 50% of the exozodiacal dust peak brightness.

## 4.3 Glint

During the starshade operation, sun rays interact with the starshade petal edges to produce glint, and increase both the noise and confusion when trying to determine the incoming signal from an Earth-like planet. In Fig. 14, the imaging performance in the presence of solar glint is examined.

We continue to explore the sun-starshade-star angle dependence, and the impact on the SNR of such glints in Fig. 15
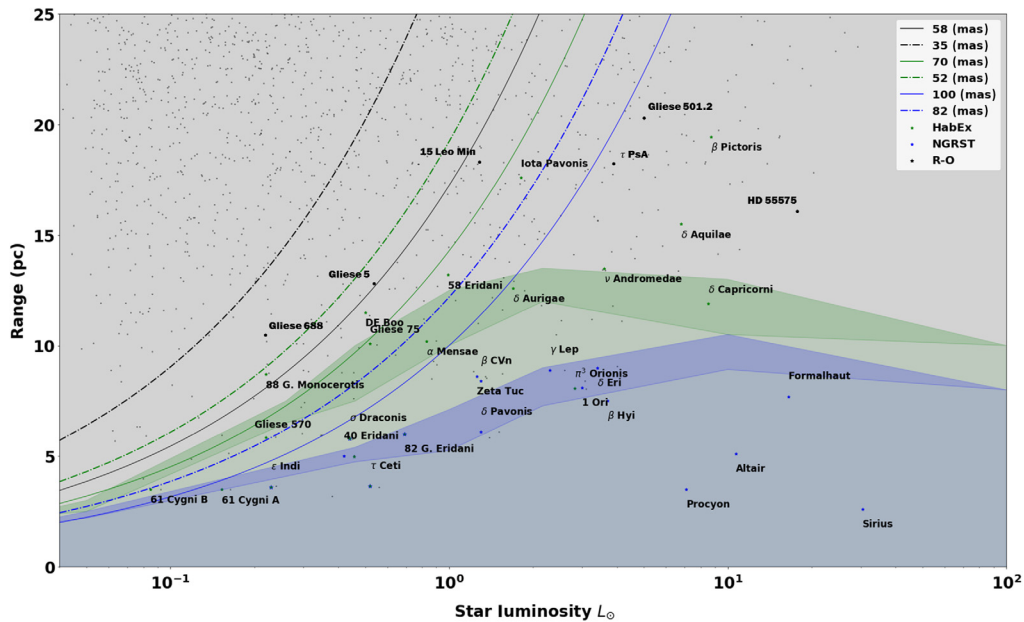
**Fig. 10** Optimistic and pessimistic implications of exo-zodi levels for a symmetrical dust distribution: The black, green, and blue curves correspond to R-O, HabEx, and NGRST, respectively. Solid curves correspond to each mission starshade IWA for a planet positioned at 1 AU scaled to the star luminosity. The dashed lines correspond to the distance at which an Earth-like planet has a completeness of 0.35 for each mission. We provide for context stars from the Gaia DR2 in gray to identify where stars are located, and the names of stars selected as potential targets for starshade missions, and the total number of stars that have habitable zones outside of the IWA of each starshade mission at the top of the image, and the number of stars within phase completeness requirement curve on the right side of the image. The semi-major axis remains constant at 1 AU scaled by luminosity, the planet radius is set to $1R_{\oplus}$, and the planetary albedo is set to 0.2.

## 4.4 *Petal Edge Error*

Petal edge effects are among the worst sources of error that could affect these observations; micrometer size deviations across meters in length could reduce the resultant contrast levels. In Fig. 16, we explore the sensitivity of missions to such perturbations, display before and after images to indicate its impact, and examine the SNR as response a function of the perturbation size.

# 5 Discussion and Conclusions

While Sec. 3 and Sec. 4 provide insight into the impact of individual parameter changes on imaging capabilities, this section integrates all explored parameters. By doing so, providing a more realistic observational scenario, enabling us to better asses the accessible target ranges and establish suitable requirements to meet each mission's scientific needs.

## 5.1 *Performance Envelopes*

In this section, we present each mission concept's cumulative range of optimistic and pessimistic observable targets as established by our sensitivity analyses. Mission deliverables are mapped according to the target star distance and luminosity in Fig. 17. The optimistic observation scenario assumes favorable conditions for imaging, exo-zodi (3 zodi), large radius planets (1.4 Earth radius) with high albedo (0.5), without starshade perturbations, etc. This optimistic scenario is indicated by the upper limit of each mission's colored region. The semi-pessimistic scenario is represented by the lower bound of each colored region, for which we assume the smallest planet radius (0.6 Earth radius), exo-zodi at the three sigma limit indicated by the HOSTS survey
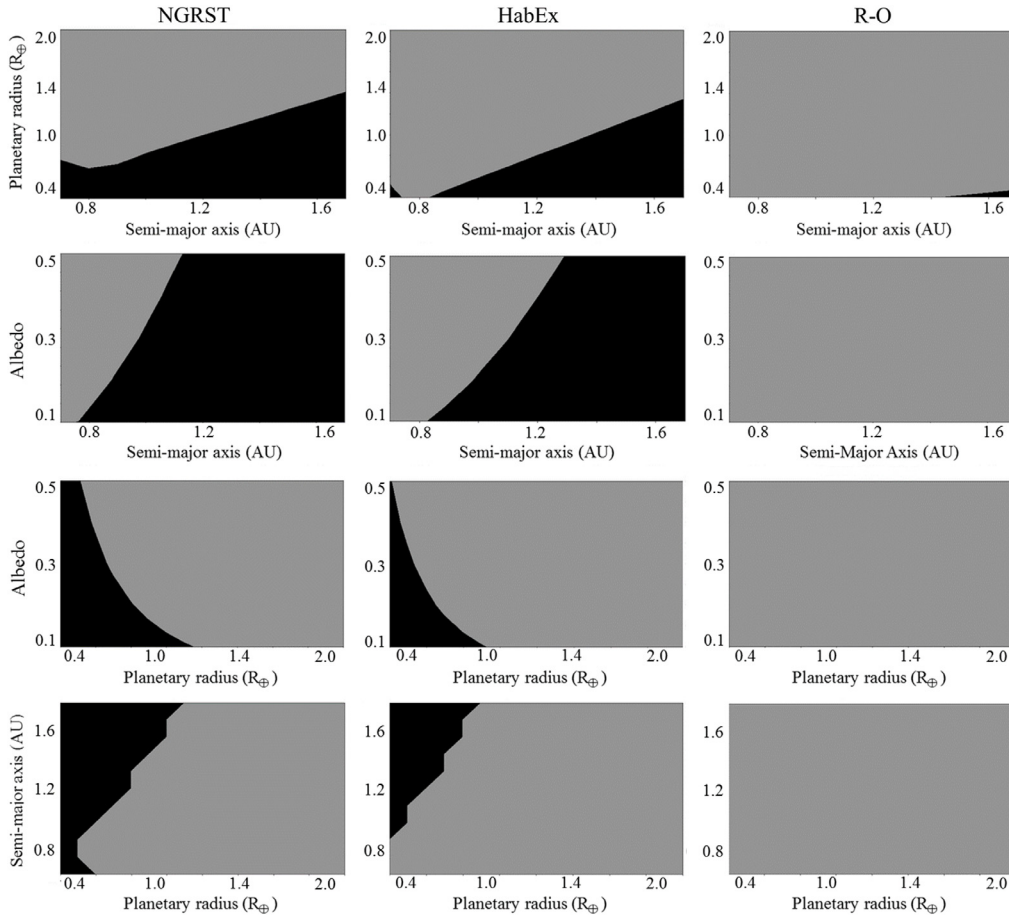
**Fig. 11** This figure contains several images that investigate how the semi-major axis, planetary radius, and planetary albedo effect image quality. To quantify the effects, we place an Earth-like planet in orbit around the star Zeta Tucanae, a G0V star located 8.6 pc away. The first three rows correspond to two of the parameters spanning across a set distance while keeping the third parameter constant. The first row has the semi-major axis on the horizontal axis (AU), the planetary radius on the vertical axis (R$_\oplus$), and a constant albedo. The second row of images has the semi-major axis on the horizontal axis, the albedo on the vertical axis, and a constant planetary radius. The third row of images has the planetary radius on the horizontal axis, the albedo on the vertical axis, and a semi-major axis held constant at 1 AU. The fourth row has the semi-major axis and planet radius spanning across the vertical and horizontal axes, respectively, but each combination of these parameters is assigned the minimum albedo required to maintain an SNR greater than or equal to 7. If the required albedo could not be established, the region was considered unreachable and denoted as black. The gray zones indicate areas where the SNR is above 7.

(21 zodi), albedo of 0.1, with starshade perturbations, etc. The dashed lines represent a shift of the exo-zodi peak brightness to 0.5 AU for all missions.

We find that even if the background noise could be perfectly calibrated, for a Sun-like star luminosity, the ranges for both the optimistic and semi-pessimistic scenarios are between 20 and 25 pc for R-O, 4.5 to 13 pc for Habex and 3 to 9 pc for NGRST. Where for stars' luminosity smaller than 1, that range decays exponentially as can be seen in Fig. 17. Needless to say, both the semi-pessimistic and optimistic predictions are in fact somewhat optimistic since perfect background calibration might not be achieved, exo-zodi levels larger than 21 could be encountered, and starshade perturbations might be larger.

## 5.2 *Detection and Confusion*

Exoplanet detection is one of the primary, simplest deliverables offered by direct imaging missions. Throughout this paper, SNR values have been calculated with pre-existing
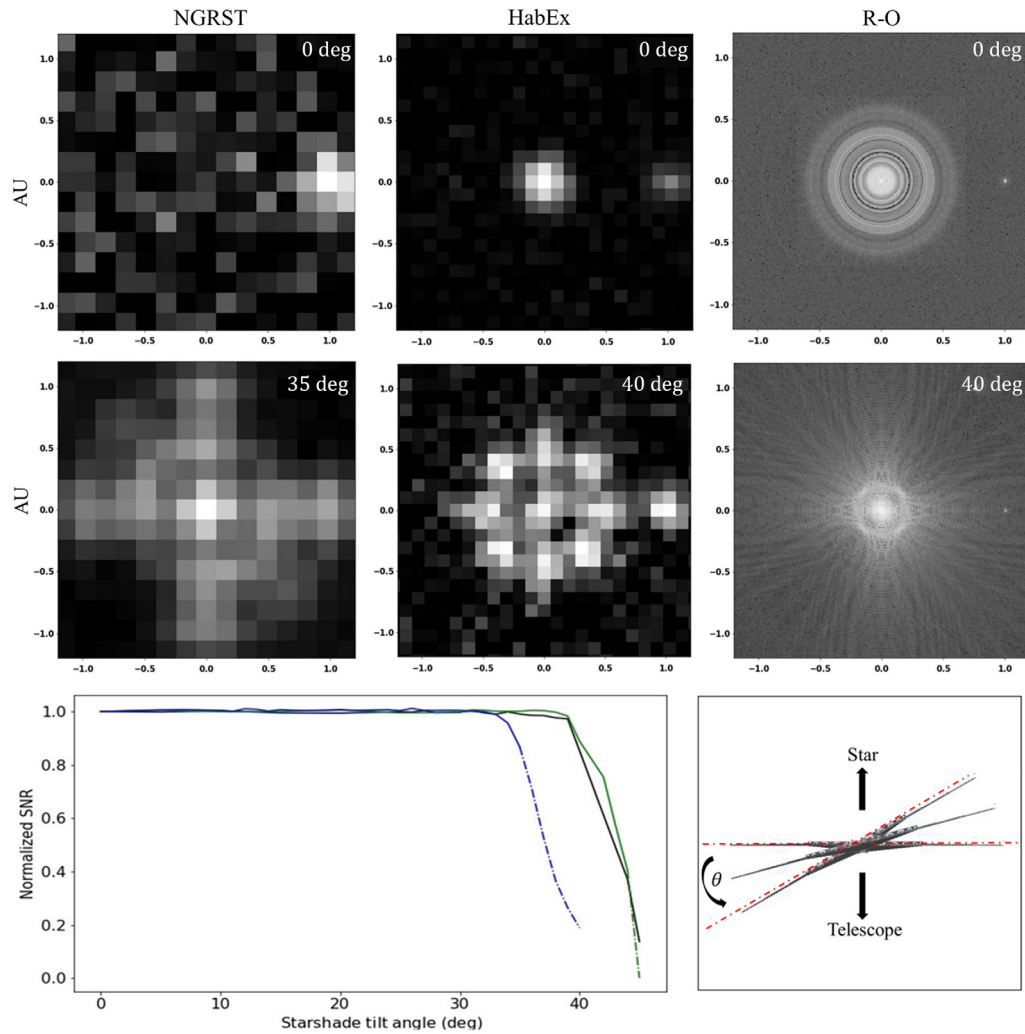
**Fig. 12** An examination of how the starshade tilt effects imaging performance for all starshade missions. The first row displays how the Beta Canum Venaticorum system would look through each telescope-starshade configuration with a 0-deg tilt. The second row shows the same astrophysical scene but with a tilt that yields poor imaging performance. The third row displays the normalized SNR of an Earth-like planet orbiting at the scaled habitable zone as a function of the starshade tilt angle. The blue, green, and black curves correspond to NGRST, HabEx, and RO, respectively. Each curve transitions into a dashed line once the actual SNR drops below 7. The cartoon on the bottom-right illustrates how the starshade tilt, identified with red arrows, changes the starshade-telescope configuration.

knowledge of target exoplanet location, size and separation among an array of other parameters. This degree of certainty will likely not be the case in future mission scenarios.

First, even when reasonable SNR levels are achieved (SNR = 7), it is challenging to identify the location of many of the planets studied in this paper. An observer must understand the predominant ensemble and system-specific background signal structures to a degree where advanced astronomical extraction and processing models can extract meaningful results. This knowledge accuracy is highly dependent on the relative and total planetary and background signal's time-varying structure. We conduct imaging simulations such that a background knowledge accuracy is assumed to be known to levels of both 1% and 5% and show in Fig. 18 at which distance and star luminosity's resultant SNR will drop below 7.

As can be seen, even if one would be able to gain a background knowledge accuracy of 1% (black), a majority of the targets will not achieve their expected SNR, which will require
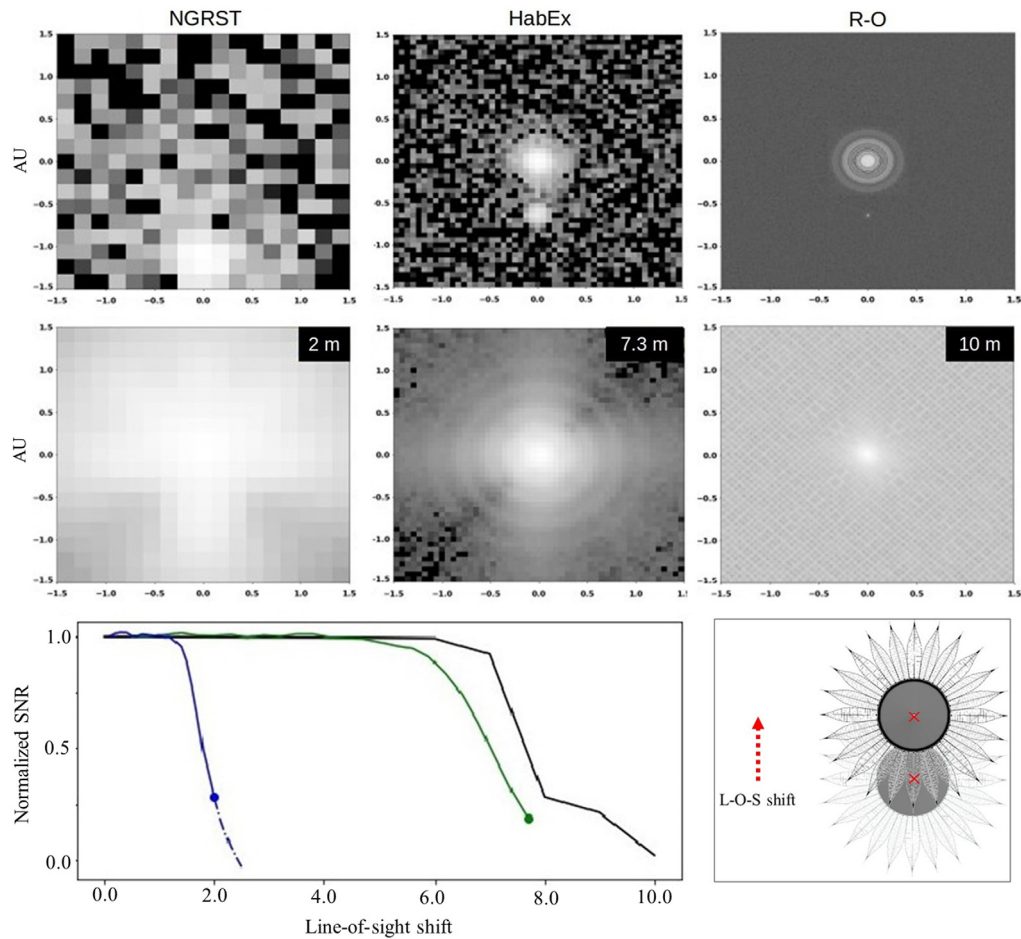
**Fig. 13** This figure investigates how the alignment of the starshade and telescope impacts the quality of images. To identify how the image quality changes, an Earth-like planet is placed in orbit around 40 Eridani A; it is a K0V star located 5 pc away. The orbit has a semi-major axis of 1 AU and it is scaled by the star's luminosity of 0.46. The top row of images are the outputs from the simulations with the ideal starshade. The second row of images are the simulations with a misaligned starshade. A significant increase in star-leakage can be seen as a result. The curves at the bottom contain the normalized SNR as a function of the line-of-sight shift in meters. NGRST, HabEx, and R-O correspond to the blue, green, and black curves, respectively. The image in the bottom right corner is a simple visualization of a starshade with a line-of-sight misalignment. In the diagram, the telescope points directly toward the starshade face on. The starshade with a dashed outline represents correct alignment, and the black starshade represents a starshade with a line-of-sight shift. For this example, the starshade is taken from NGRST and a 5-m vertical shift is applied to illustrate how the shift alters the observation setup. The red arrow points in the direction of the shift, and its length corresponds to the magnitude of the shift. The two red crosses correspond to the center of both starshades. The dashed cross is at the center of the ideal starshade, and the cross above sits at the center of the misaligned starshade.

expanding the targets exposure time (or updating the SNR requirement) to compensate for such losses. This phenomenon becomes even more prominent at a knowledge level of 5% (red), making it one of the most dominant factors to consider when coming to estimate SNR requirements for explanatory targets. This finding will have an even larger impact on other target SNR requirements like SNR = 20 for detailed spectral characterization[9] and will be driven by the available or desired integration time allocation for target stars for each mission.

We provide in Table 2 estimates for the updated required SNR for the detection of Earth-like planets with few prime targets.
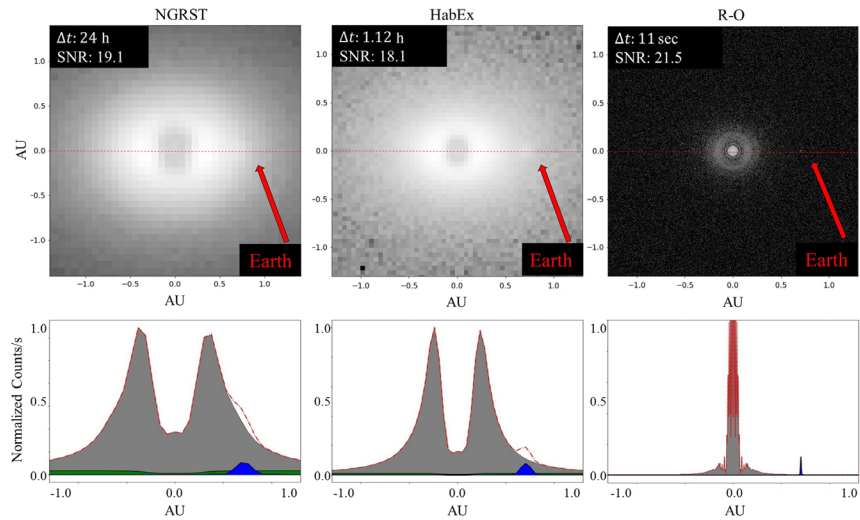
**Fig. 14** This figure returns to Tau Ceti, but with the addition of solar glint to investigate how it impacts the simulated data and resulting images. The star-starshade-sun angle was set to 65 deg for all three starshade missions. These simulations can be seen in the top row. The three curves in the bottom row come from a horizontal slice taken from the images in the top row capturing the star leakage, exozodiacal dust, solar glint, local zodiacal dust, noise, and the planet flux. The gray region is the combined background flux from the star and exozodi dust, the green region is the local zodiacal dust, and the blue region is the planet flux. The dashed red line is the combination of the planet and background flux. All exposure times and SNR values can be seen in the top left corner of each image.
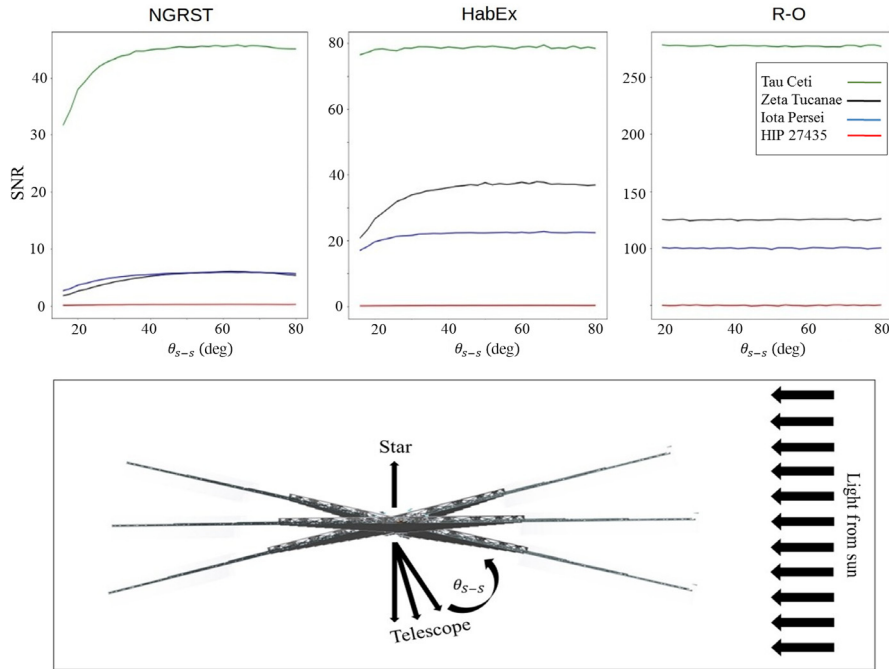


**Fig. 15** The three images above illustrate how solar glint effects the SNR of Earth-like planets. The effect on an Earth-like planet's SNR as solar glint is applied to all three starshade missions. The brightness of the glint corresponds to the angle between the starshade and sun spans from 15 deg to 80 deg. For each mission, three stars are shown: Tau Ceti in green, Zeta Tucanae in black, Iota Persei in blue, and HIP 27435 in red. These are G8V, G0V, G0V, and G4V stars with a distance of 3.65, 8.6, 10.5, and 15.2 pc, respectively. These simulations did not contain any exozodiacal dust but did contain the local zodiacal dust from our solar system. For each star, the semi-major axis of Earth's orbit was scaled by each star's luminosity. For all stars, Earth was placed in a 1 AU orbit and scaled by the luminosity of each star.
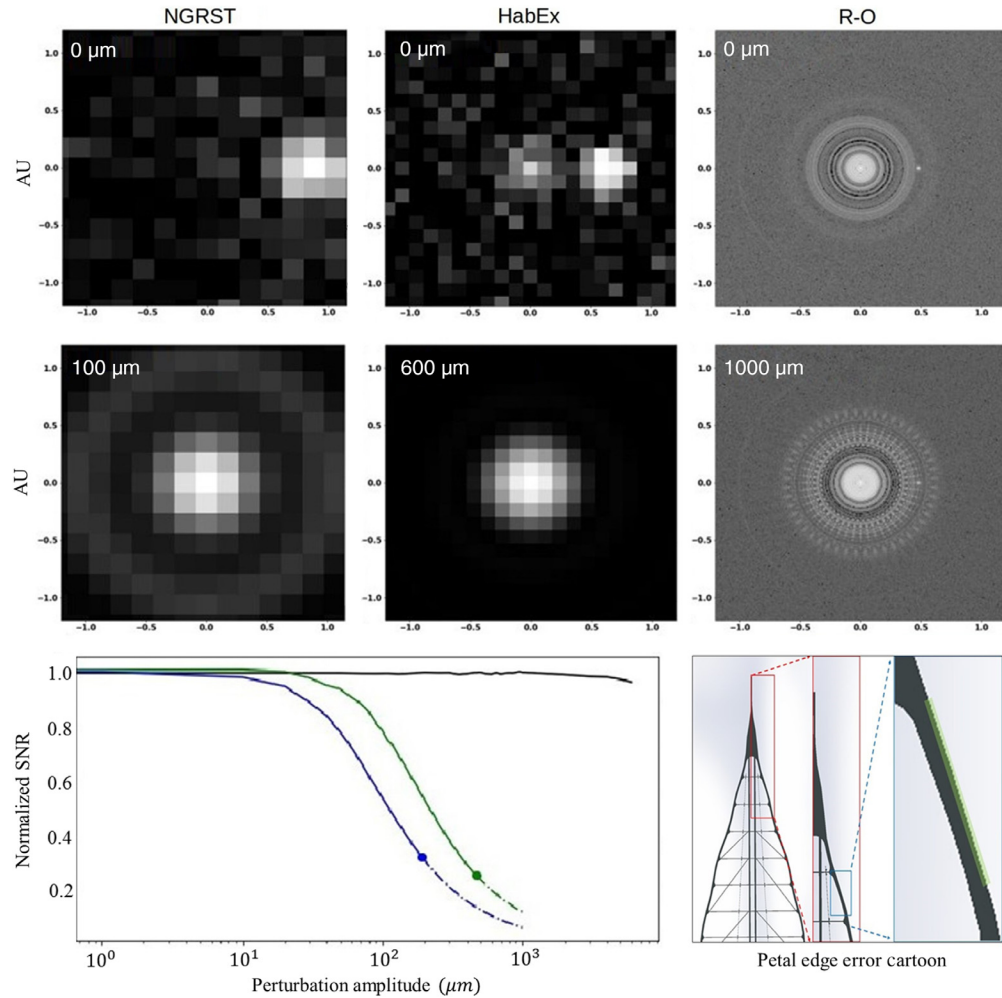
**Fig. 16** This figure analyzes how imperfections present on the petals of each starshade effects the resulting SNR of a planet. In each simulation, 40 Eridani A was chosen as the target star, and it has a distance of 5 pc, has a luminosity of $0.46\,L_\odot$, and it is a K0V star. An Earth-like planet was placed in an orbit with a semi-major axis of 1 AU scaled by the luminosity of 40 Eridani A. The exozodi factor was set to 0, and solar glint was turned off. The first row of images contains the final simulation for all three starshade missions with ideal starshades for NGRST, HabEx, and R-O, respectively. The second row contains the final simulated image using starshades that have a perturbation along the edges of all petals. An increase in star-leakage can be seen as a result. The curves at the bottom are the normalized SNR as a function of perturbation amplitude. The amplitude spans from 1 to 6000 $\mu$m. NGRST, HabEx, and R-O are shown in blue, green, and black, respectively. Once the SNR drops below 7, the curve transforms into a dashed line. The cartoon on the bottom-right illustrates the edge-errors applied to the RO starshade

Second, in Fig. 19 we assess the missions ability to disentangle the signal of an earth-like planet from a nearby planet at different separations. We define planets being fully inseparable (90% of the signal of both planets overlaps), confused (10% to 90% of the signal overlaps), and separable (90% of the signal is not overlapping).

We find that even under ideal conditions, small planets (Super Earth or smaller) separated by <60, 40, and 5 mas and large planets (Jupiter, etc.) separated by <100, 90, and 10 mas, will be confused or outright inseparable for NGRST, HabEx, and R-O, respectively. These findings, however, do not account for less favorable observation conditions and other systematic or background signal sources such as resonant dust bulbs and moons, which are expected to enlarge the required minimal separation range to avoid confusion.
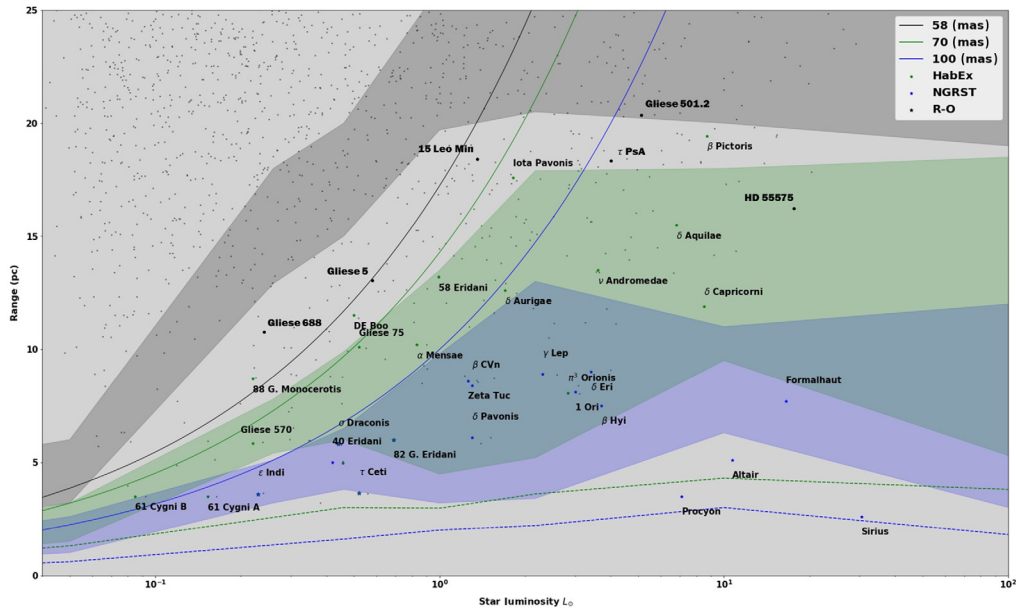
**Fig. 17** SISTER-simulated accessible ranges of mission-specific target stars. NGRST, HabEx, and R-O are marked in purple, green, and black, respectively. The top and bottom edge of each colored region correspond to the optimistic and semi-pessimistic scenario for each mission. The pessimistic scenario is marked by a dashed line.
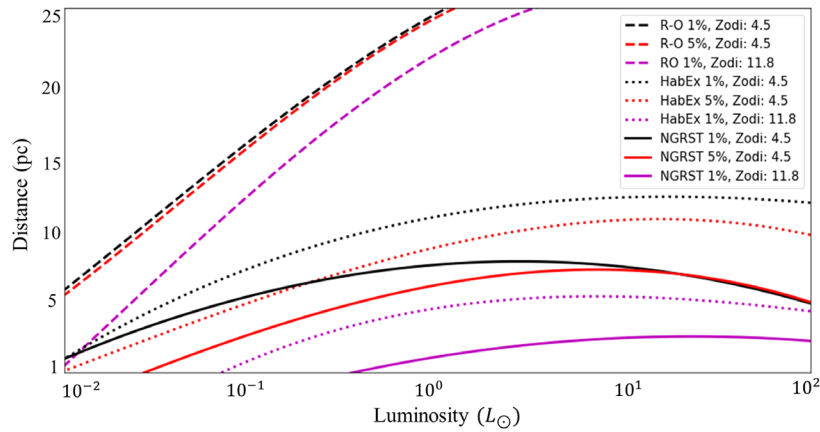


**Fig. 18** The maximum distance each mission can observe as a function of Luminosity for two different background knowledge levels. The three black and red curves correspond to 1% and 5%, respectively with an exozodi factor of 4.5. The magenta curves correspond to an exozodi level of 11.8 with a 1% background knowledge.

**Table 2** NGRST and HabEx SNR requirements with 1% background knowledge for three high priority target stars.

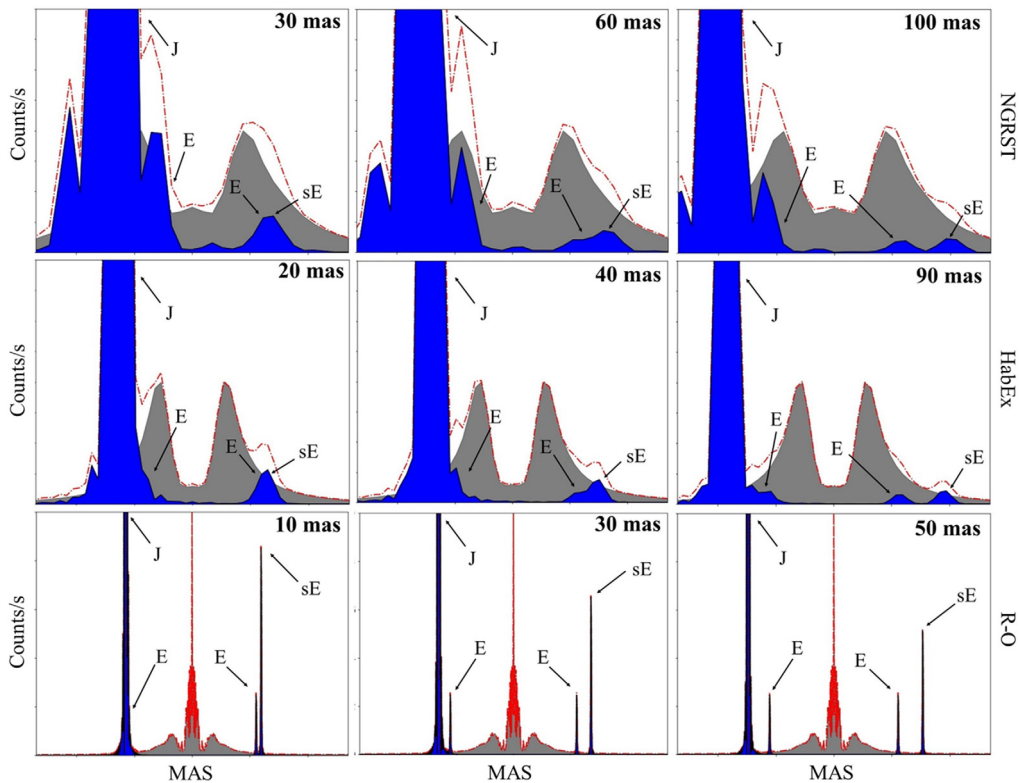| Star | NGRST 1% | HabEx 1% |
|---|---|---|
| Tau Ceti | >30 | >10.0 |
| Zeta Tucanae | >30 | >10 |
| 72 Herculis | >60 | >13 |

**Fig. 19** Two combinations of planets are explored to identify how the angular separation of planets affects signal identification. The two combinations are Earth and Jupiter, and Earth and a super Earth where the radius is $2R_\oplus$. For each combination, there are three different angular separations depending on the starshade mission. The first column corresponds to an angular separation where the planets cannot be distinguished because the signals combine into a single peak. The second column identifies the angular separation where you can begin to distinguish the planets from one another. The third column corresponds to the separation that yields two distinguishable peaks for the planets. However, the signal for the Earth-like planet close to Jupiter remains washed out even at 100 mas.

### 5.3 *Toward a Realistic Exoplanet observation Scenario*

A realistic model of starshade observation should account for a variety of possible starshade perturbations and exo-planetary environments. In Fig. 20, we show for 40 Eridani A, a K0V star located 5 pc away, for the three missions, the evolution of an ideal image as we introduce a starshade line of sight shift of 0.5 m, 70 $\mu$m edge error, and solar glint, along with exo-zodi level of 7, and our local zodi dust. We presented for each image the resultant SNR and required noise knowledge in percent.

By examining Fig. 20, one can easily see that the observations could become extremely challenging even for nearby stars. To assess the impact of these perturbing factors on target stars completeness values, we perform a statistical study of ensemble SNR 7 threshold observability based on full end-to-end optical simulations for various missions and target stars. These results are given in Table 3

For each mission and star, C0 represents previously establish completeness values, C1 is produced by running 4000 end-to-end optical simulations by pulling system parameters from the observational priors and distributions described in Sec. 3 and Appendix B. Including all the natural parameters studied in this paper, C2 integrates starshade perturbations as described in Sec. 4. Finally, C3 accounts for a background knowledge accuracy of 1%.

As can be seen, even for short and moderate distances, the completeness values for each target and mission are negatively impacted. These results, however, do not indicate that starshade-based missions produce lower completeness values compared to a coronagraph for
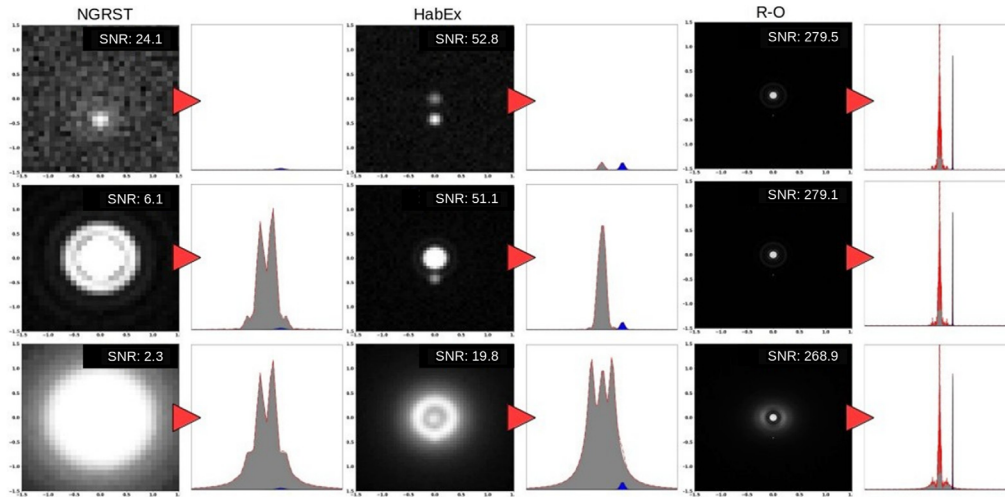
**Fig. 20** Three simulations of image weakening observational perturbations for 40 Eridani A, a K0V star located 5 pc away. We show first the simulations with ideal conditions; there is no exozodi within the system, no solar glint, and no local zodi dust. In the second row, we introduce starshade imperfections: 0.5 m LOS shift and 70 $\mu$m errors on all petal edges. In the bottom row, we further applied an exozodi factor of 7, turned on solar glint and local zodi dust. The SNR for an Earth-like planet orbiting at 1 AU scaled by 40 Eridani A's luminosity of 0.45 assuming a 1% background knowledge level is shown in the top right corner of each image. The exposure time for NGRST, HabEx, and R-O are 24 h, 10 h, and 30 min, respectively.

**Table 3** A list of completeness values from prime starshade mission targets. Each target possesses multiple completeness $C_N$ values, which correspond to a different completeness. $C_1$ is the our standard completeness solution computed within SISTER. $C_2$ is the completeness with an additional source of background flux coming from a line of sight error and petal edge error on the starshade. $C_3$ is the completeness when we require the background knowledge equal to 1%. NGRST and HabEx both contain a $C_0$ value, and it corresponds to completeness values from previous reports as a reference.

| HIP | Name | $L_\odot$ | $D$ (pc) | NGRST | | | | HabEx | | | | R-O | | |
|---|---|---|---|---|---|---|---|---|---|---|---|---|---|---|
| | | | | $C_0$ | $C_1$ | $C_2$ | $C_3$ | $C_0$ | $C_1$ | $C_2$ | $C_3$ | $C_1$ | $C_2$ | $C_3$ |
| 8102 | Tau Ceti | 0.45 | 3.65 | 0.67 | 0.67 | 0.64 | 0.48 | 0.89 | 0.84 | 0.83 | 0.81 | 0.96 | 0.96 | 0.96 |
| 19849 | 40 Eridani | 0.457 | 4.985 | 0.65 | 0.521 | 0.50 | 0.26 | 0.92 | 0.70 | 0.69 | 0.66 | 0.912 | 0.91 | 0.90 |
| 96100 | Sigma Draconis | 0.410 | 5.76 | 0.55 | 0.45 | 0.44 | 0.20 | 0.825 | 0.63 | 0.61 | 0.58 | 0.88 | 0.88 | 0.88 |
| 99240 | Delta Pavonis | 1.24 | 6.108 | 0.64 | 0.60 | 0.57 | 0.21 | 0.83 | 0.72 | 0.72 | 0.70 | 0.91 | 0.91 | 0.91 |
| 61317 | Beta CVN | 1.151 | 8.44 | 0.43 | 0.39 | 0.34 | 0.06 | 0.81 | 0.56 | 0.54 | 0.52 | 0.89 | 0.88 | 0.87 |
| 1599 | Zeta Tucanae | 1.26 | 8.60 | 0.42 | 0.39 | 0.34 | 0.05 | 0.81 | 0.56 | 0.55 | 0.51 | 0.87 | 0.87 | 0.87 |

example. It is merely an indication of the maturity level of new end-to-end optical models, and a more complete understanding of the challenges facing future direct imaging missions.

## 5.4 *Future Work*

Future work will include an investigation into starshade-based spectral characterization capabilities and an expansion on the study of resonant dust rings and structure and their impact on detection capabilities. A study of the impact of other systematic non-planetary noise and signal

sources (expanded from photo-metric noise limitations provided in this paper) will follow. Additional work will be conducted to generate target lists and case by case mission and target star selections, and SISTER-based multi-parameter optimization of starshades for their specific paired observatory. Finally, we aim to utilize insights provided in this paper to better understand their impact on the scientific yield and quality of an array of starshade missions.

## 6 Appendices

### 6.1 *Appendix A: Applying Starshade Perturbations*

SISTER performs high fidelity simulations of directly imaged exoplanets by considering both the detector, telescope, and the design of the starshade to create a PSF spatial response. All of these considerations are stored within files that SISTER reads and compiles before creating a simulation. For starshades, the design is stored within three individual arrays corresponding to each dimension ($X$, $Y$, and $Z$).

The first perturbation we discuss is a starshade with a tilt, meaning that there is a relative angle between the starshade's plane and the telescope. To create the necessary optical response of this new starshade configuration, a new file containing the starshade design is required. The new $X$, $Y$, and $Z$ arrays can be computed by performing a simple rotation about the $X$ or $Y$ axis. Then assign this file to be the new starshade you desire to use for the simulation, and a new PSF will be built.

Starshades that possess an off-line of sight error were simple to create. The values within the starshade design files have units in meters, so we simply add or subtract a constant value to either the $X$ or $Y$ array. This will force SISTER to build a new PSF because the starshade is no longer centered within the simulations.

Petal edge errors are the most complicated perturbations to apply. We applied sinusoids across the perimeter of each starshade corresponding to different frequencies, amplitudes, and phases. We elected to use an array of amplitudes, and a frequency of 1 amplitude per meter.

### 6.2 *Appendix B: System Parameters*

When we establish system parameters for our simulations, we either select parameters that match the Solar System, or we select from a range of values to create synthetic systems containing Earth-like planets. These ranges will be briefly summarized. The range of planetary radii corresponds to rocky worlds capable of maintaining an atmosphere. The range of orbital radii corresponds with established inner[22] and outer[23] habitable zone ranges. Each orbital radius drawn from this range scales as $\sqrt{L_*}$. The inclination of the orbits follows a normal cosine distribution. We assume all planets are spheres following a Lambertian phase function with an albedo ranging from 0.1 to 0.5 averaging around an Earth-like albedo of 0.3. Finally, the exozodi level present within the system corresponds to a factor that is multiplied to the standard zodi level of the system, which we assume has a surface brightness of 23 mag/arcsecond$^2$.[16] The HOSTS[21] survey provided optimistic and pessimistic exozodi levels, which we adopted when selecting our range. A summary of all values can be found in Table 1.

## Acknowledgments

## References

1. National Research Council, *New Worlds, New Horizons in Astronomy and Astrophysics*, The National Academies Press, Washington DC (2010).

2. W. Cash, "Analytic modeling of starshades," *Astrophys. J.* **738**, 76 (2011).
3. R. J. Vanderbei, E. Cady, and N. J. Kasdin, "Optimal occulter design for finding extrasolar planets," *Astrophys. J.* **665**, 794–798 (2007).
4. D. Mawet et al., "Review of small-angle coronagraphic techniques in the wake of ground-based second-generation adaptive optics systems," *Proc. SPIE* **8442**, 62–82 (2012).
5. J. R. Males and O. Guyon, "Ground-based adaptive optics coronagraphic performance under closed-loop predictive control," *J. Astron. Telesc. Instrum. Syst.* **4**(1), 019001 (2018).
6. E. National Academies of Science and Medicine, *Exoplanet Science Strategy*, The National Academies Press, Washington DC (2018).
7. Y. Fujii et al., "Exoplanet biosignatures: observational prospects," *Astrobiology* **18**, 739–778 (2018).
8. S. Seager et al., "Starshade rendezvous probe mission," Bulletin of the AAS51, https://baas.aas.org/pub/2020n7i106 (2010).
9. B. S. Gaudi et al., "The Habitable Exoplanet Observatory (HabEx) mission concept study final report," (2020).
10. F. Patat, O. S. Ugolnikov, and O. V. Postylyakov, "Orbiting configurable artificial star (orcas) for visible adaptive optics from the ground," *Astron. Astrophys.* **51**, 385–393 (2006).
11. J. Mather et al., "Orbiting starshade:observing exoplanets at visible wavelengths with gmt, tmt, and elt," *Bull. Am. Astron. Soc.* **51**, 48 (2020).
12. E. Peretz, "Exoplanet imaging scheduling optimization for an orbiting starshade working with extremely large telescopes," *J. Astron. Telesc. Instrum. Syst.* **7**(2), 021213 (2021).
13. E. Peretz et al., "Mapping the observable sky for a Remote Occulter working with ground-based telescopes," *J. Astronom. Telesc. Instrum. Syst.* **7**(2), 021212 (2021).
14. S. R. Hildebrandt et al., "SISTER: starshade imaging simulation toolkit for exoplanet reconnaissance," *J. Astron. Telesc. Instrum. Syst.*, to be submitted (2021).
15. E. Cady, "Boundary diffraction wave integrals for diffraction modeling of external occulters," *Opt. Express* **20**, 15196–15208 (2012).
16. S. Hildebrandt and S. Shaklan, "SISTER handbook," https://docs.google.com/document/d/1_Cu6D_yYCNfFx1ZxAQbTt3WCcmO1j9MY-6VVvvLG2dU/edit#heading=h.j66bhhm3dapg (2020).
17. R. Morgan et al., "The standard definitions and evalu-360ation team final report: a common comparison of exoplanet yield," 2019, http://https://exoplanets.nasa.gov/exep/studies/sdet/.
18. A. Roberge et al., "The exozodiacal dust problem for direct observations of exo-earths," *Publ. Astron. Soc. Pac.* **124**, 799–808 (2012).
19. S. F. Dermott, "A circumsolar ring of asteroidal dust in resonant lock with the earth," *Nature* **369**, 719–723 (1994).
20. W. T. Reach et al., "Observational confirmation of a circumsolar dust ring by the cobe satellite," *Nature* **374**, 521–523 (1995).
21. S. Ertel, "The hosts survey for exozodiacal dust: Observational results from the complete survey," *Astron. J.* **159**, 177 (2020).
22. R. M. Ramirez and L. Kaltenegger, "A volcanic hydrogen habitable zone," *Am. Astron. Soc.* **837**(1).
23. R. K. Kopparapu et al., "Habitable zones around main-sequence stars: new estimates," *Astrophys. J.* **765**, 131 (2013).

**Eliad Peretz** is a technology program manager and leads the small sat development lab at Goddard Space Flight Center. He received his PhD in mechanical aerospace engineering with a minor in applied physics from Cornell University and has been with GSFC since 2015.

**Kevin Hall** is currently an astrophysics research assistant within the Department of Astronomy at the University of Maryland. He received his BS degree in astronomy and physics in 2019.

**John C. Mather** is the senior project scientist on the James Webb Space Telescope. He is also a senior astrophysicist in the Observational Cosmology Laboratory located at NASA's Goddard Space Flight Center.

**Stuart Shaklan** is the supervisor of the High Contrast Imaging Group in the Optics Section of the Jet Propulsion Laboratory. He received his PhD in optics at the University of Arizona in 1989 and has been with JPL since 1991.

**Sergi Hildebrandt** is a scientist at the Jet Propulsion Laboratory and lecturer at the California Institute of Technology. He received his PhD in theoretical physics at the University of Barcelona. He has worked in the data analysis of the cosmic microwave background from space and ground missions, adaptive optics in the visible, and more recently on leading the development of SISTER, a user friendly, open source project that generates starshade simulations with very high fidelity.